



DEPARTMENT OF PHYSICS

---

---

Master's degree in Advanced Methods in Particle Physics

# CHARACTERISATION OF SILICON STRIP SENSORS

*Supervisor:*  
M.Sc. Michael Windau

*Lab report of:*  
Giulio Giamello  
Cem Kurt

Summer Semester 2025



# Contents

<b>Introduction</b>	<b>1</b>
<b>1 Theory: semiconductor detectors</b>	<b>2</b>
1.1 Electronic band structure . . . . .	2
1.2 Semiconductors . . . . .	3
1.3 Doping of semiconductors . . . . .	4
1.3.1 n-type semiconductors . . . . .	5
1.3.2 p-type semiconductors . . . . .	5
1.4 The pn-junction . . . . .	6
1.5 Interaction of ionising radiation with matter . . . . .	8
1.5.1 The beta decay . . . . .	9
1.5.2 interactions of electrons in matter . . . . .	10
1.6 Pedestals and Noise . . . . .	11
<b>2 Experimental setup</b>	<b>13</b>
2.1 Detector unit . . . . .	13
2.2 Laser . . . . .	15
2.3 Control unit . . . . .	15
<b>3 Measurement process and analysis</b>	<b>17</b>
3.1 Depletion voltage . . . . .	18
3.2 Pedestal run . . . . .	18
3.3 Calibration measurements . . . . .	20
3.4 Characteristics of the strip sensor . . . . .	23
3.5 Charge Collection Efficiency . . . . .	26
3.5.1 CCEL (laser) . . . . .	27
3.5.2 CCEQ (beta source) . . . . .	28
3.6 Large source scan . . . . .	30
<b>Conclusions</b>	<b>33</b>



# Introduction

Silicon detectors represent a cornerstone technology in particle physics experimentation. Their predominant application lies in tracking systems designed to precisely reconstruct the trajectories of charged particles. Additionally, they function as active sensing elements within sampling calorimeters for specific experimental configurations. This calorimetric application is anticipated to gain significance due to the growing demand for high-granularity calorimeters essential for particle flow reconstruction methodologies [?].

In this project, the characteristics of a silicon strip sensor and its readout electronics are examined with a Educational Alibava System (EASy) [?], through systematic irradiation using two distinct sources. Initial calibration employs a laser source to establish baseline detector response under controlled, well-defined conditions. Subsequently, a radioactive isotope replaces the laser to emulate realistic detection scenarios. The selected isotope, strontium-90 ( $^{90}\text{Sr}$ ), undergoes  $\beta^-$  decay, producing yttrium-90 ( $^{90}\text{Y}$ ) as a daughter nucleus. This  $^{90}\text{Y}$  isotope itself decays via  $\beta^-$  emission to stable zirconium-90 ( $^{90}\text{Zr}$ ), forming a two-stage decay chain. [Figure 1](#) details this sequence, including the half-lives ( $T_{1/2}$ ) of both isotopes and the maximum kinetic energies ( $\beta_{1,\text{max}}$ ,  $\beta_{2,\text{max}}$ ) of the emitted electrons.

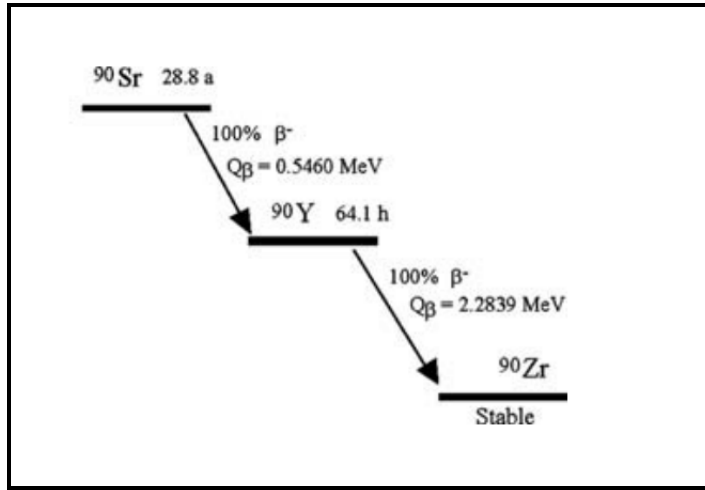


**Figure 1:** Decay chain of the isotope  $^{90}\text{Sr}$ , from [?].

As both decay stages generate electron emissions, their energy spectra are recorded concurrently. The substantial separation between the characteristic endpoint energies of the  $^{90}\text{Sr}$  and  $^{90}\text{Y}$  decays allows for clear spectroscopic discrimination and independent analysis of the two electron distributions.

# Chapter 1

## Theory: semiconductor detectors

In order to understand a silicone strip detector it is important to look at the theory of semiconductors.

### 1.1 Electronic band structure

Introduction to energy band theory in crystals.

X-ray analysis and other research have revealed that most metals and semiconductors possess a *crystalline structure*, meaning an ordered atomic arrangement that repeats regularly in space. When forming this structure, the energy levels of electrons are altered. As atoms bond to form a crystal, the energy levels of the outermost shell electrons change most significantly since these electrons are shared between multiple atoms through covalent bonds.

The energy levels of these electrons can be determined through quantum mechanics. Specifically, electrons occupy not isolated single levels but *bands* of allowed energies. The interval between a band's maximum and minimum energy is called the "band width". Energy bands can be: valence bands, conduction bands, or forbidden bands.

The valence band is occupied by electrons shared between multiple atoms in the crystal, i.e., the band containing electrons farthest from the nucleus. The conduction band is the first empty band above it. Valence and conduction bands are separated by the "forbidden band", an energy interval where no electrons can exist, whose width is typically denoted by  $E_g$  ("energy band gap").

As the distance between atoms in the crystalline structure decreases, the width of the forbidden band narrows until the conduction band overlaps with the valence band. The energy separation between valence and conduction bands determines whether materials are classified as insulators, semiconductors, or metals.

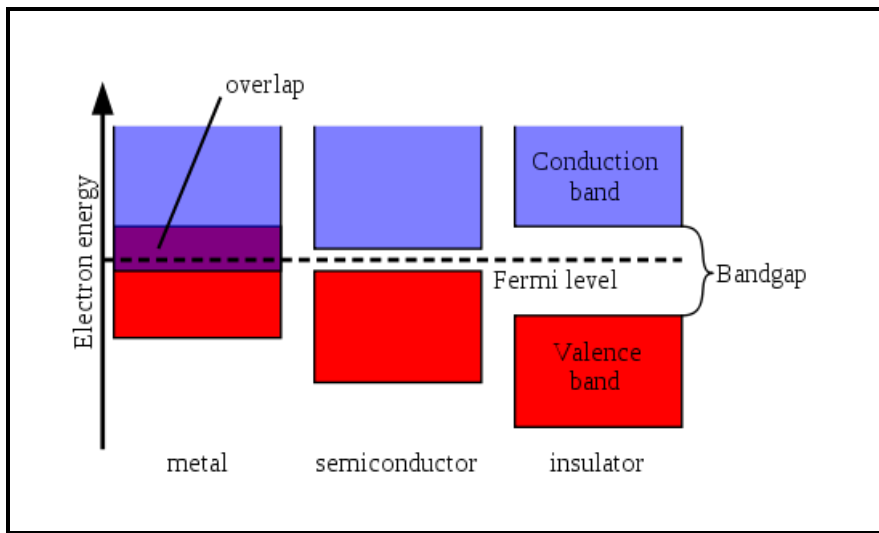


**Figure 1.1:** Energy band distribution in a metal, semiconductor, and insulator.

Insulators are materials where the forbidden band is wider than the energy an electron can acquire from an external field, preventing electrons from reaching the conduction band. Conversely, conductors have no forbidden band, with valence and conduction bands overlapping. This allows electrons to move freely to higher energy levels under an external field.

Finally, materials where valence and conduction bands neither overlap nor are separated by an impassable forbidden band (energetically) are called *semiconductors*.

## 1.2 Semiconductors

In electronic components (e.g., diodes), the most common semiconductors are germanium [Ge] and silicon [Si]. At 0 K, these have  $E_g \approx 0.785$  eV and  $E_g \approx 1.21$  eV respectively – values exceeding the energy an electron typically gains from an external field to reach the conduction band. Thus, at this temperature, Ge and Si behave as insulators since no electron has sufficient energy to cross the band gap.

As temperature increases, some electrons gain thermal energy  $> E_g$  and transition to the conduction band. These are called *free electrons*, and the material becomes a *semiconductor* due to its mobile charge carriers. Note that semiconductor conductivity increases with temperature, as higher temperatures generate more free electrons (charge carriers).

When an electron moves to the conduction band, it leaves an empty energy state in the valence band called a *hole*. Thus, each electron in the conduction band corresponds to one hole in the valence band.

**def.** A *intrinsic semiconductor* satisfies:

$$p = n$$

where p is hole concentration (valence band) and n is electron concentration (conduction band).

If  $p \neq n$ , it is an *extrinsic or doped semiconductor*.

### 1.3 Doping of semiconductors

Doping involves adding small percentages of trivalent or pentavalent impurity atoms to an intrinsic semiconductor to alter hole/electron density, creating an extrinsic semiconductor.

(Ge and Si atoms are tetravalent)

- **Donors:** Pentavalent atoms added to the semiconductor (e.g., phosphorus [P]). When bonding with lattice atoms, they form covalent bonds using four of their five valence electrons. The fifth electron remains mobile, becoming a charge carrier. Donor doping is called *n-type*, as it increases electrons and decreases holes (compared to intrinsic values).
- **Acceptors:** Trivalent atoms added to the semiconductor (e.g., boron [B]). These form covalent bonds with only three of the semiconductor's four valence electrons, leaving a hole in the fourth bond. Acceptor doping is called *p-type*.

The semiconductor material utilized in this investigation is silicon, characterized by a band gap energy of 1.107 eV at room temperature [?]. Silicon atoms possess four valence electrons and crystallize in a diamond cubic lattice configuration. Within this structure, electron vacancies (holes) emerge when valence electrons are displaced through thermal excitation or external particle interactions. These vacancies exhibit quasi-particle behaviour with an effective positive charge.

When subjected to an external electric field, established via cathode/anode contacts, the formation of bound electron-hole pairs (excitonic states) is suppressed. Under such bias conditions, liberated electrons and holes become mobile charge carriers that migrate toward the respective anode and cathode.

The electrical properties of silicon can be deliberately engineered through doping, a controlled substitutional process wherein host lattice atoms are replaced with impurity atoms possessing different valence electron counts. This atomic substitution modifies the charge carrier concentrations and transport characteristics.

### 1.3.1 n-type semiconductors

When silicon is doped with pentavalent impurities (e.g., arsenic, possessing five valence electrons), four electrons participate in covalent bonding with adjacent silicon atoms. The fifth electron remains weakly bound to its parent atom, requiring minimal energy (typically  $< 0.05$  eV) to enter the conduction band as a mobile charge carrier. This process generates excess negative charge carriers without creating corresponding vacancies in the valence band.

### 1.3.2 p-type semiconductors

Doping with trivalent elements (e.g., boron, having three valence electrons) creates electron deficiencies in the crystal lattice. Each impurity atom forms incomplete covalent bonds with neighbouring silicon atoms, resulting in localized positive charge regions. These sites readily accept valence electrons from adjacent atoms, effectively generating mobile positive charge carriers known as holes that propagate through the lattice.

[Figure 1.2](#) schematically illustrates both doping mechanisms and their distinct effects on charge carrier generation in crystalline silicon.

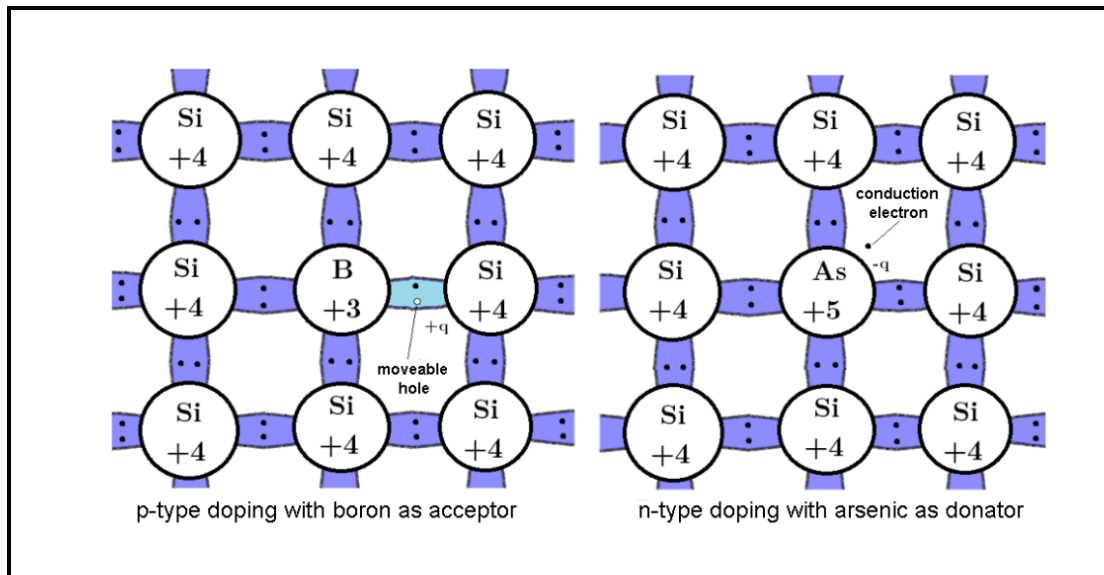


**Figure 1.2:** Graphical representation of boron and arsenic doping in silicon.

## 1.4 The pn-junction

The p-n junction is the contact region between p-type and n-type semiconductors, namely a *diode*.

Electrons (holes) approach the junction due to mutual attraction, leaving electrically neutral zones ( $\rho = 0$ ) at the far right (left) of the diode. The resulting central region is called the

depletion region: a zone divided by the junction with thickness 0.5 microns. Near the junction, high hole concentration in the p-region and low concentration in the n-region cause holes to diffuse from p to n, while electrons diffuse from n to p. This charge flow constitutes the diffusion current  $I_d$  (direction: p to n). (Depletion width depends on doping and is inversely proportional to doping density on each side).

Recombination starts at the junction and expands the depletion region until electron hole attraction can no longer overcome it. When the depletion width reaches equilibrium (where attraction is insufficient), recombination stops, leaving unrecombined “uncovered charges” on both sides. Thus, near the junction: the p-material has a region depleted of holes containing exposed negative charges, while the n-material has exposed positive charges.

This creates:

- $\rho = 0$  at the junction due to recombination;
- $\rho > 0$  on the n-side (peak at positive uncovered charges);
- $\rho < 0$  on the p-side (minimum at negative uncovered charges).

This charge distribution generates an electric field (flux lines: positive  $\rightarrow$  negative uncovered charges) and a *diffusion voltage*  $U_D$  opposing further diffusion. The depletion potential acts as a barrier that holes/electrons must overcome to diffuse into n/p-material respectively. Thus,  $I_d$  depends on  $V_d$ , as the potential barrier height affects the number of free carriers and diffusion current.

To enable detection of ionizing radiation, an external bias voltage is applied across the diode terminals. Under reverse bias conditions:

- Electrons from the negative terminal recombine with holes in the p-type region
- Electrons in the n-type region migrate toward the positive terminal

This charge carrier migration creates a charge-neutral region devoid of mobile carriers, known as the *depletion zone*. The width  $d(U)$  of this zone depends on the applied voltage  $U$  according to:

$$(1.1) \quad d(U) = \sqrt{\frac{2\epsilon(U_D + U)}{eN_{\text{eff}}}}$$

where:  $\epsilon$  denotes the dielectric constant of silicon,  $e$  is the elementary charge and  $N_{\text{eff}}$  represents the effective charge carrier density.

The effective charge carrier density is determined by the dopant densities in each region:

$$(1.2) \quad N_{\text{eff}} = \frac{N_D N_A}{N_D + N_A}$$

with  $N_D$  and  $N_A$  being the donor (n-type) and acceptor (p-type) densities, respectively.

When the depletion zone spans the entire diode thickness  $D$ , full depletion occurs at the characteristic *depletion voltage*  $U_{\text{dep}}$ . This threshold voltage is approximated by:

$$(1.3) \quad U_{\text{dep}} \approx \frac{eN_{\text{eff}}D^2}{2\epsilon}$$

The depletion depth  $d_c(U)$  exhibits distinct behaviour in two voltage regimes, characterized by the relationship:

$$(1.4) \quad d_c(U) = \begin{cases} D \sqrt{\frac{U}{U_{\text{dep}}}} & \text{for } U < U_{\text{dep}} \\ D & \text{for } U \geq U_{\text{dep}} \end{cases}$$

This functional dependence demonstrates that below the depletion voltage ( $U < U_{\text{dep}}$ ), the active detection region expands proportionally to the square root of the applied voltage. Once  $U$  reaches or exceeds  $U_{\text{dep}}$ , the depletion zone spans the entire diode thickness, saturating at  $d_c = D$ . This transition marks the optimal operating condition for radiation detection.

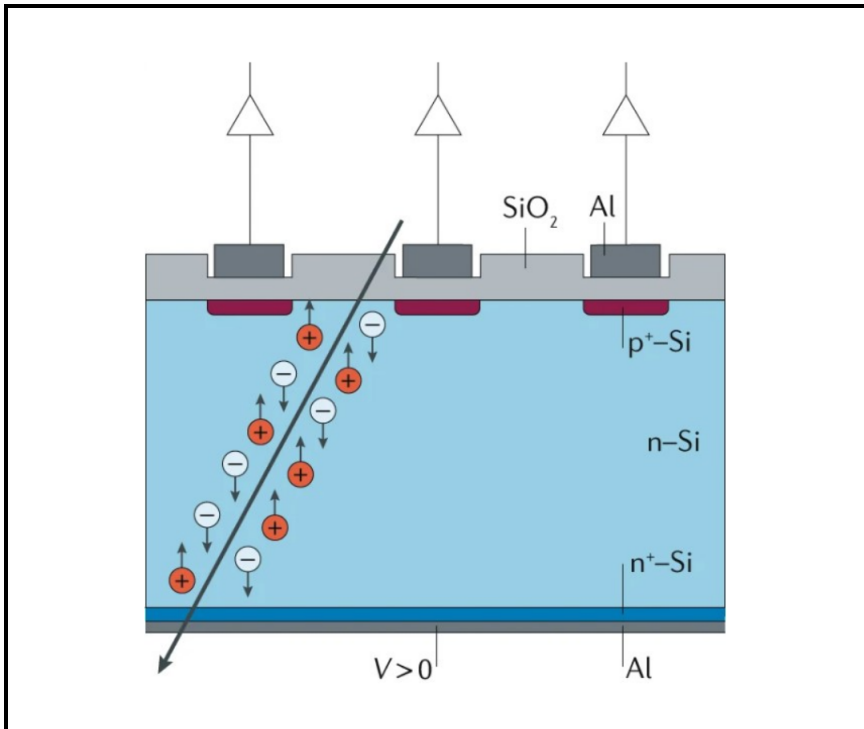


**Figure 1.3:** Silicon strip detector crossed by a charged particle, from [?].

## 1.5 Interaction of ionising radiation with matter

For effective detection of ionizing radiation, the diode should ideally operate in a fully depleted state. This condition maximizes the active detection volume, ensuring particle-induced charge carriers generate measurable signals. However, thermal excitation processes can promote electrons into the conduction band even without radiation, producing a *leakage current*.

The magnitude of this leakage current exhibits strong voltage dependence, increasing monotonically with applied bias. The characteristic current-voltage relationship for the detector diode is presented in Figure 2, which illustrates the transition between partial and full depletion regimes.

The depletion voltage ( $U_{\text{dep}}$ ), marking the onset of full depletion, can be determined through analysis of the current-voltage characteristics shown in Figure 1.4. This critical operational parameter corresponds to the voltage where the depletion region spans the entire diode thickness.

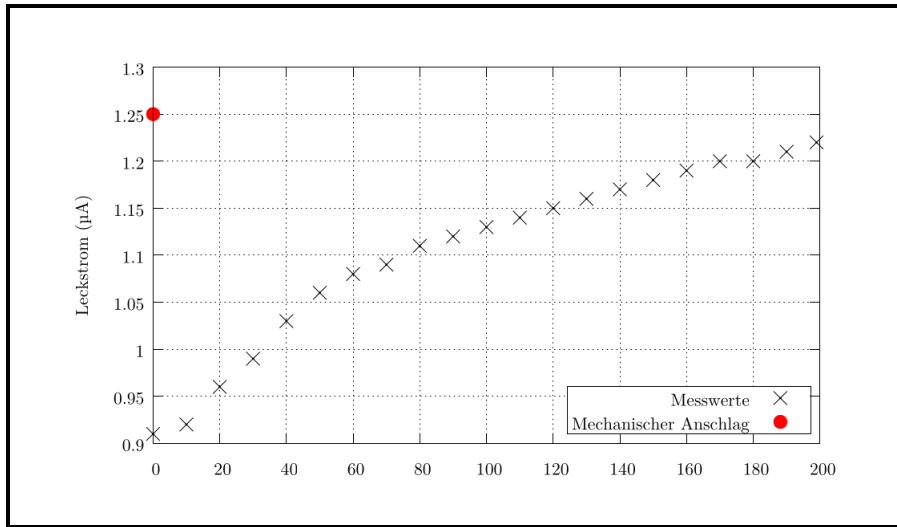


**Figure 1.4:** Current-voltage characteristic curve of the Educational Alibava system. The depletion voltage  $U_{\text{dep}}$  can be estimated from the flattening of the curve at 60 V. Note that the adjustment knob for the bias voltage is not turned to the mechanical stop, as here the voltage is applied minimally in the forward direction, which leads to the value marked in red.

The silicone strip detector can be used to detect ionizing particles. During the experiment a source producing beta particles is employed.

### 1.5.1 The beta decay

The primary radiation source utilized in this experiment is the  ${}^{90}\text{Sr}$  isotope, which undergoes  $\beta^-$  decay according to the following sequence:



This decay chain produces two distinct  $\beta^-$  emissions:

- ${}^{90}\text{Sr} \rightarrow {}^{90}\text{Y}$  transition:  $E_{\beta,\text{max}} = 0.545 \text{ MeV}$
- ${}^{90}\text{Y} \rightarrow {}^{90}\text{Zr}$  transition:  $E_{\beta,\text{max}} = 2.28 \text{ MeV}$

During  $\beta^-$  decay, a nuclear neutron transforms into a proton through the weak interaction process:



This three-body decay mechanism results in a continuous energy distribution for the emitted electrons, as the available  $Q$ -value is partitioned variably among the electron, antineutrino, and recoil nucleus. The characteristic energy spectrum for  $\beta^-$  decay electrons is shown in Figure 1.5.

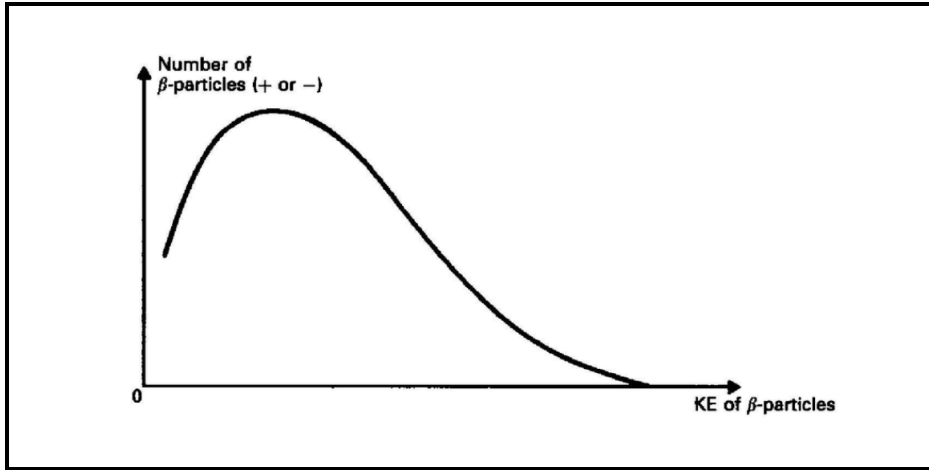


**Figure 1.5:** Electron energy spectrum of a  $\beta^-$  decay, from [?].

The temporal decay behaviour is quantified by the *activity*  $A$ , defined as the disintegration rate:

$$(1.7) \quad A \equiv -\frac{dN}{dt} = \lambda N_0 e^{-\lambda t} = A_0 e^{-\lambda t}$$

where  $\lambda$  denotes the decay constant,  $N_0$  the initial number of radioactive nuclei, and  $A_0$  the initial activity.

### 1.5.2 interactions of electrons in matter

Low-energy electrons ( $E < 3$  MeV) predominantly lose energy through Coulomb interactions with atomic nuclei within the detector material. These ionizing collisions excite bound electrons in the semiconductor's crystalline lattice, producing electron-hole pairs that generate measurable detection signals. The average energy deposition per unit path length for relativistic electrons is described by the modified Bethe-Bloch formula:

$$(1.8) \quad -\frac{dE}{dx} = 2\pi N_a m_e c \rho \frac{Z}{A} \frac{1}{\beta^2} \left[ \ln \left( \frac{\tau^2(\tau + 2)}{2(I/m_e c^2)^2} \right) + F(\tau) - \delta - 2 \frac{C}{Z} \right]$$

with the auxiliary function:

$$(1.9) \quad F(\tau) = 1 - \beta^2 + \frac{\frac{\tau^2}{8} - (2r_e + 1) \ln(2)}{(\tau + 1)^2}$$

where  $\tau = \gamma - 1$ ;  $\gamma$  is the Lorentz factor, and other parameters follow standard particle physics notation.

For electrons originating from the  ${}^{90}\text{Sr}$  decay spectrum, this formulation yields an average energy loss of 3.88 MeV/cm in silicon.

The statistical distribution of energy deposition events differs significantly with detector thickness. While bulk detectors ( $\gtrsim 1$  mm) exhibit approximately Gaussian energy loss distributions, thinner devices (such as the  $300\ \mu\text{m}$  detector employed here) demonstrate substantial deviations from normal statistics. In such thin absorbers, the energy loss distribution follows a Landau distribution, characterized by asymmetric broadening and a pronounced high-energy tail.

This distribution is further modified by the inherent energy spectrum of  $\beta$ -decay electrons, resulting in a convolution of the Landau distribution with the continuous  $\beta$  energy spectrum. The composite energy deposition profile for our experimental configuration is presented in [Figure 1.6](#).

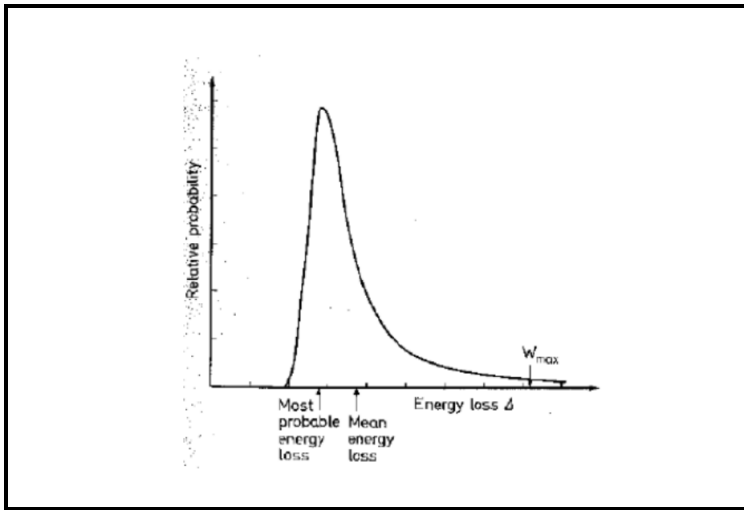


**Figure 1.6:** Convoluted Landau distribution, describing the energy deposition of electrons in a  $300\ \mu\text{m}$  silicon sensor.

## 1.6 Pedestals and Noise

All electronic measurement systems, including radiation detectors, exhibit inherent noise that obscures the desired signal. In this experiment, the charge deposition is

given in counts of the Analog-to-Digital Converter (ADC) and therefore has to be converted to keV on the basis of a calibration measurement. For strip detectors interfaced with an ADC, the digitized output for strip  $i$  during measurement  $k$  follows:

$$(1.10) \quad \text{ADC}(i, k) = P(i) + D(k) + S(i, k)$$

where:

- $S(i, k)$  represents the true physical signal;
- $P(i)$  denotes the *pedestal* (baseline offset) for strip  $i$ ;
- $D(k)$  signifies the *common mode shift* affecting all strips during measurement  $k$ .

The pedestal  $P(i)$  is determined as the mean ADC response in the absence of physical signals:

$$(1.11) \quad P(i) = \frac{1}{N} \sum_{k=1}^N \text{ADC}(i, k)$$

where  $N$  represents the number of noise measurements.

The common mode shift  $D(k)$  quantifies system-wide electronic fluctuations and is computed via:

$$(1.12) \quad D(k) = \frac{1}{128} \sum_{i=1}^{128} [\text{ADC}(i, k) - P(i)]$$

The intrinsic electronic noise per strip is characterized by the RMS deviation:

$$(1.13) \quad \sigma(i) = \sqrt{\frac{1}{N-1} \sum_{k=1}^N [\text{ADC}(i, k) - P(i) - D(k)]^2}$$

This noise parameter  $\sigma(i)$  provides the fundamental resolution limit for detecting physical signals on strip  $i$ .

# Chapter 2

## Experimental setup

The measurement system employs an Alibava EASy radiation detection platform comprising three primary components:

1. **Detector unit:** Silicon microstrip sensor assembly
2. **Control unit:** Signal processing and interface electronics
3. **Data acquisition computer:** System control and analysis

Interconnections between components are established through:

- Ribbon cable (detector  $\leftrightarrow$  control unit)
- USB interface (control unit  $\leftrightarrow$  computer)
- Optional optical fiber for specialized measurements

System operation is managed through the Alibava Graphical User Interface (GUI), which provides:

- Real-time detector control
- Measurement configuration
- Data visualization and acquisition

In some measuring tasks, an additional optical fiber cable is used. In the source measurements, a radioactive source ( $^{90}\text{Sr}$ ) and a LEMO cable for the built-in diode are needed.

### 2.1 Detector unit

The detector unit employs a semiconductor sensor integrated with dedicated readout electronics. Positioned above the sensor assembly, a configurable laser system provides controlled excitation for signal generation. This laser features two operational orientations: the “L” position facilitates laser-based calibration measurements, while the “Q” position enables radioactive source characterization.

Signals generated within the sensor undergo amplification and processing through the BEETLE application-specific integrated circuit which converts charge pulses into

digitizable voltage waveforms. The BEETLE chip incorporates a pipeline buffer that temporarily stores processed signals until receipt of an external trigger command from the control unit. Only triggered events are transmitted for further analysis; untriggered data streams are systematically discarded to optimize data throughput.

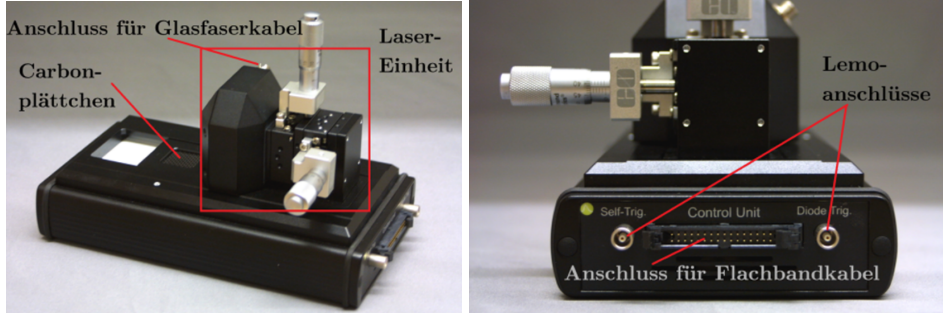


**Figure 2.1:** The detector unit in “Q” position. Top view (left) and side view (right).

The detection element consists of a  $300\ \mu\text{m}$  thick n-doped silicon substrate. One surface features a continuous metallization layer, while the opposite face contains 128 electrically isolated p-doped strip implants. This configuration establishes a p-n junction architecture, specifically categorized as a p-in-n sensor due to the p-type implants embedded within the n-type bulk material. Electrical isolation between adjacent strips prevents inter-strip conduction, enabling spatial resolution of incident radiation through channel-specific signal readout. A silicon oxide layer suppresses surface leakage currents that could compromise signal integrity.

The sensor incorporates two critical peripheral structures: a guard ring that confines charge carriers within the active detection area, and a bias ring that applies the operational voltage to establish the depletion zone. [Figure 2.1](#) illustrates the detector unit in the "Q" configuration, while [Figure 2.2](#) provides detailed schematics of the sensor geometry.

Application of reverse bias voltage ( $U_{\text{bias}}$ ) generates an internal electric field that separates electron-hole pairs created by ionizing events. Below the depletion threshold, significant carrier recombination occurs in undepleted regions, degrading signal amplitude. The charge collection efficiency (CCE) quantifies this behaviour according to:

$$(2.1) \quad \text{CCE}(U) = \frac{1 - \exp\left(-\frac{d_c(U)}{a}\right)}{1 - \exp\left(-\frac{D}{a}\right)}$$

where  $D = 300 \mu\text{m}$  is the sensor thickness,  $d_c(U)$  represents the voltage-dependent depletion depth, and  $a$  denotes the mean laser penetration depth in silicon. CCE increases monotonically with applied voltage until reaching full depletion at  $U_{\text{dep}} \approx 60\text{--}70 \text{ V}$ , beyond which it plateaus at maximum efficiency. For electron excitation measurements, signal amplitude scales directly with  $d_c(U)$ .

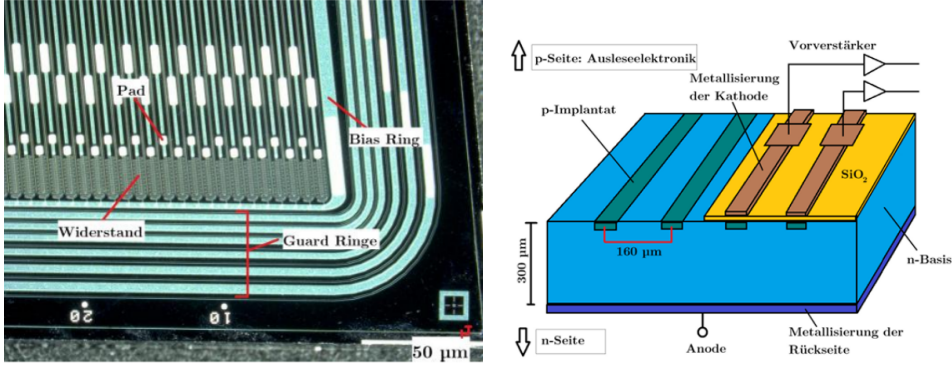


**Figure 2.2:** Macroscopic top down view (left) and a schematic view of the construction of the whole sensor (right).

## 2.2 Laser

The experimental setup incorporates a dedicated laser system for detector calibration. This laser source operates at 980 nm wavelength and delivers optical pulses to the detector unit through a fiber-optic interface. Key beam parameters include a 20  $\mu\text{m}$  spot diameter, 5 ns pulse duration, and 0.2 mW peak optical power.

Precise spatial control of the laser illumination is achieved via a dual-axis micrometer screw assembly, enabling accurate positioning and focal adjustment on the sensor surface. This calibration subsystem provides controlled localized excitation for characterizing detector response and spatial resolution.

## 2.3 Control unit

The control unit serves as the central interface for detector operation, providing three primary functions: laser illumination control, sensor bias voltage regulation, and signal acquisition. This unit processes raw detector outputs into digital ADC counts that are subsequently recorded by the data acquisition computer. Additionally, it incorporates an amperometer capable of measuring leakage currents with a resolution of 0.01  $\mu\text{A}$ .

To discriminate between noise and events detection, a statistical threshold is applied. For this experiment, signals must exceed the noise floor by at least five standard deviations ( $5\sigma$ ) to be considered valid. Events failing this signal-to-noise criterion are excluded from further analysis.

Further signal integrity challenges arise from spatial effects within the strip detector geometry. When ionizing particles traverse near strip boundaries, induced charge may trigger multiple adjacent strips despite originating from a single physical event. This edge effect is compounded by crosstalk phenomena, where non-perpendicular particle trajectories deposit charge across several strips. Both effects necessitate sophisticated position reconstruction algorithms to correctly identify individual particle interactions.

The control unit's integrated measurement capabilities extend to continuous monitoring of sensor leakage currents. Processed ADC data streams are transmitted via USB to the acquisition computer, where the Alibava software platform enables data collection and system control.

# Chapter 3

## Measurement process and analysis

Prior to data acquisition, comprehensive familiarization with both the hardware setup and Alibava software interface is essential. The measurement sequence initiates with a systematic current-voltage characterization of the sensor, recording leakage current at 10 V intervals from 0 V to 200 V beyond the anticipated depletion voltage. The software-based measurements commence with a *pedestal run* (1000 events) to determine the pedestal and the noise.

Before using the laser or the radioactive source, a set of calibration measurements are started. The first calibration is used to determine the optimal delay. It is started using the *Delay measurement* button in the Alibava software. After this run, five different channels are used in a *Calibration run*, with the applied voltage above the depletion voltage.

Another run is started afterwards with the applied voltage turned down to 0 V.

For laser-based measurements, the laser is lead into the detector unit using the optic fiber cable. It is then synchronized for timing calibration using the *laser sync* function. Then the structure of the sensor is probed by recording 1000 events at 35 discrete positions (10  $\mu\text{m}$  intervals). Charge Collection Efficiency (CCE) characterization is performed through voltage-dependent measurements (0-200 V in 10 V steps, 1000 events per setting).

Radioactive source measurements follow an analogous protocol but with enhanced statistics: 10,000 events per voltage step during CCE scans. The experiment concludes with a high-statistics source measurement recording 1,000,000 events for large scan analysis.

### 3.1 Depletion voltage

The first measurement of the analysis is the current-voltage characteristic curve of the silicon strip sensor. Figure 3.1 presents the measured leakage current as a function of applied bias voltage. The characteristic curve exhibits a flattening at 60 V, that corresponds to the depletion voltage  $U_{\text{dep}} = 60$  V. To ensure stable operation under full depletion conditions during subsequent measurements, the bias voltage was maintained at 80 V.

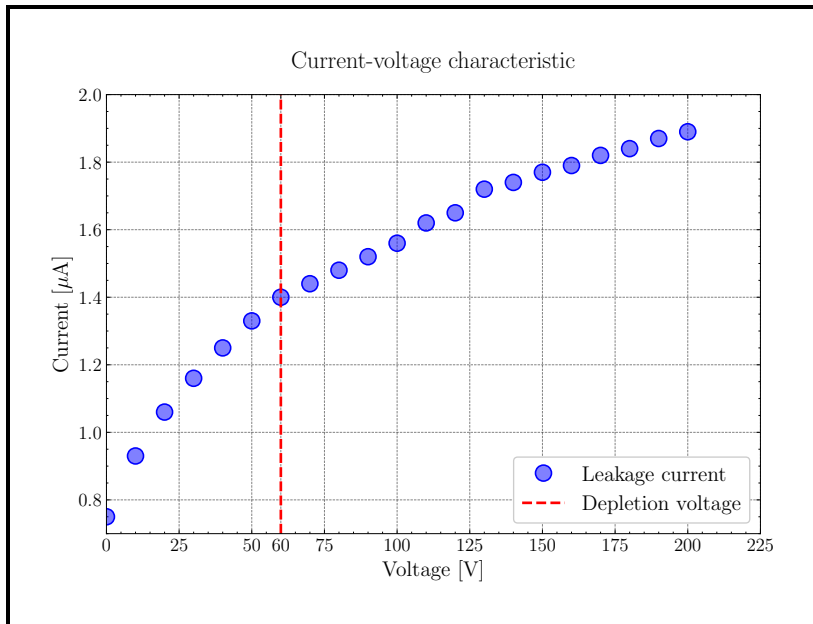
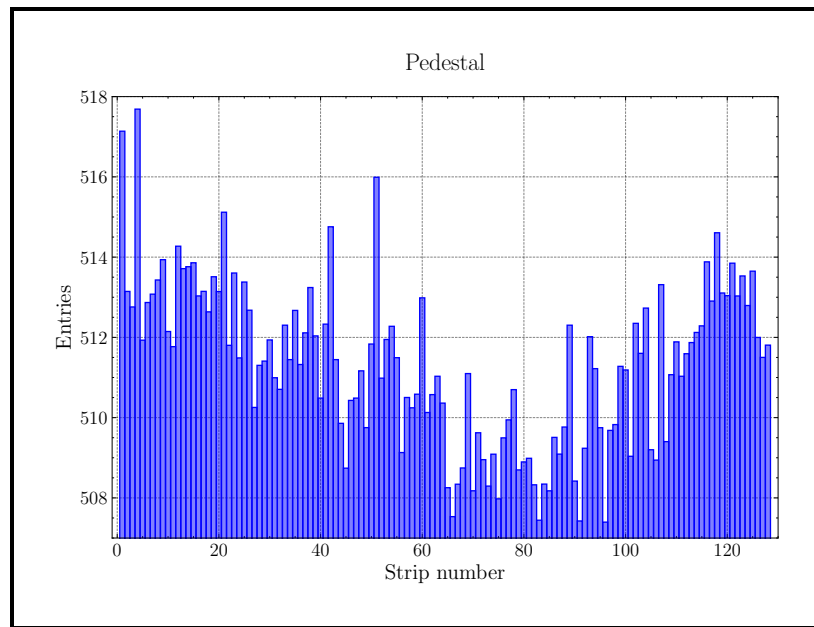


Figure 3.1: Plot of the measured current-voltage characteristic.

### 3.2 Pedestal run

The pedestal run data provides the basis for quantifying strip detector noise. For each strip, the pedestal value  $P(i)$  is computed as the arithmetic mean of ADC counts across all events, consistent with equation (1.11). Subsequent processing determines the common mode shift  $D(k)$  for individual events by first subtracting the ADC counts of each strip and again taking the mean value according to equation (1.12).



**Figure 3.2:** Bar diagrams of the pedestal of the 128 individual strips.

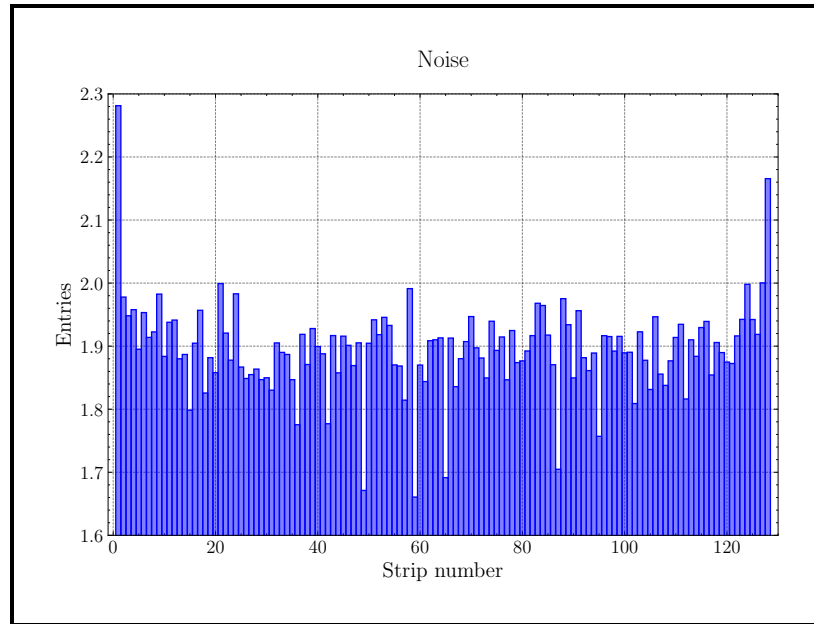


**Figure 3.3:** Bar diagrams of the noise of the 128 individual strips.

The electronic noise  $\sigma(i)$  for each strip is derived through application of [equation \(1.13\)](#), which incorporates both the pedestals and common mode corrections. This

noise parameter represents the fundamental resolution limit for signal detection in each channel.

[Figure 3.2](#) and [Figure 3.3](#) present the spatial distribution of pedestal and noise values across the detector array. Both parameters exhibit pronounced elevation near the chip periphery, because of the structure of the chip or the way the signal is read out.

The common mode shift distribution, displayed in [Figure 3.4](#), demonstrates the expected Gaussian profile centered at zero. This confirms the stochastic nature of system-wide electronic fluctuations and validates the common mode correction methodology.

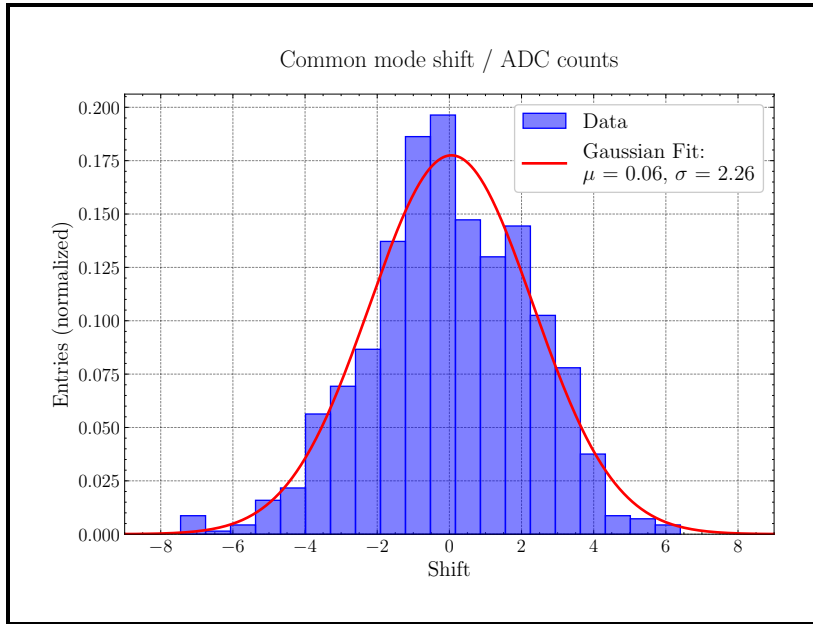


**Figure 3.4:** Common mode shift measured during the pedestal run.

### 3.3 Calibration measurements

[Figure 3.5](#) shows the ADC counts depending on the delay of the chip readout: the maximum signal amplitude occurs at 64 ns delay, establishing this as the optimal setting for subsequent experimental measurements.

Following timing optimization, charge injection calibration was performed across five representative channels. The resulting calibration curves, presented in [Figure 3.6](#), demonstrate the relations between injected charge and ADC response. As one can see in [Figure 3.7](#), an additional curve at 0 V is recorded for channel 80 and compared to the regular curve of this channel.

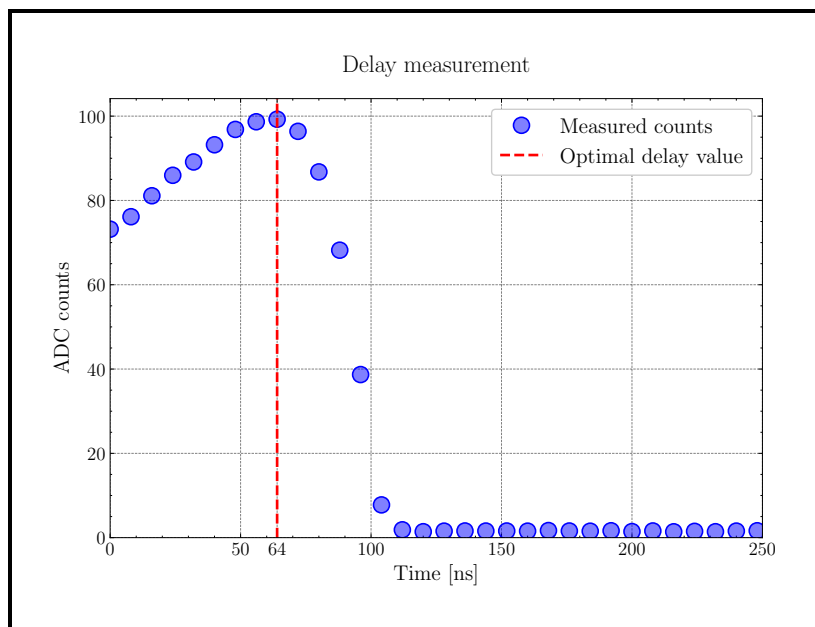


**Figure 3.5:** Strength of the signal as function of the delay time. The red line highlights the optimal one (64 ns).

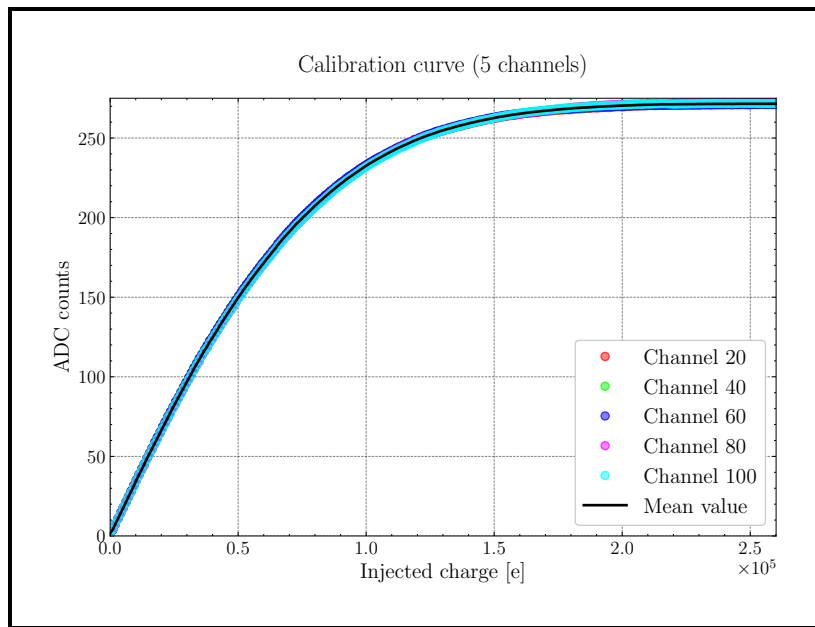


**Figure 3.6:** Calibration curve of five channels.

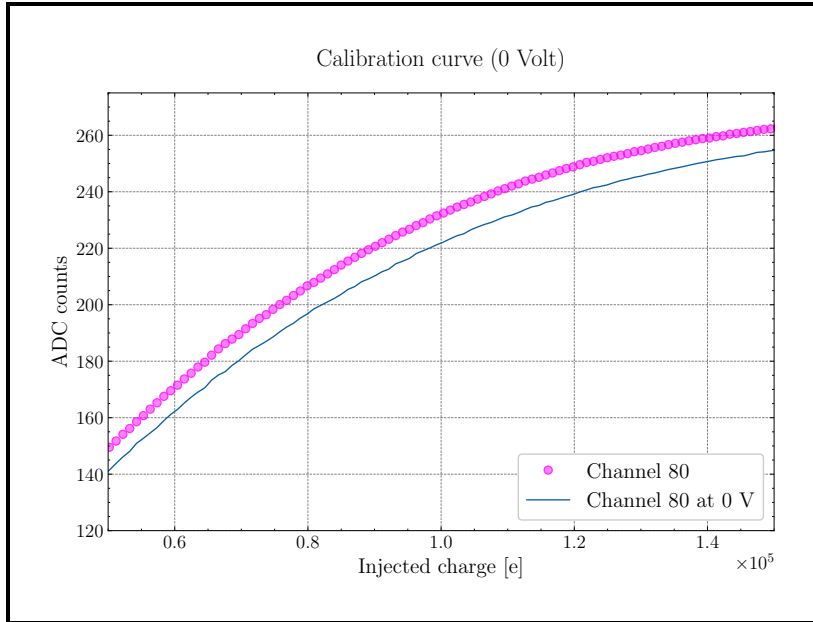


**Figure 3.7:** Detailed view of channel 80 at 0 V.

As showed in [Figure 3.6](#), the calibration profiles exhibit remarkable consistency across all channels. The average of the five channels reveals a systematic voltage dependence: measurements at 0 V bias yield lower calibration values compared to those above the depletion voltage. This expected behaviour stems from the reduced depletion region width at zero bias, which decreases charge collection efficiency and thereby reduces registered ADC counts, as confirmed in [Figure 3.7](#).

To quantitatively characterize the charge response, a fourth-order polynomial was fitted to the mean ADC values:

$$(3.1) \quad Q(\text{ADC}) = a \cdot \text{ADC}^4 + b \cdot \text{ADC}^3 + c \cdot \text{ADC}^2 + d \cdot \text{ADC} + e$$

where  $Q$  represents the injected charge. Optimal fitting required restricting the analysis to the domain below 250 ADC counts, as higher values introduced non-linear effects that reduce model accuracy. The resulting calibration function is presented in [Figure 3.8](#).

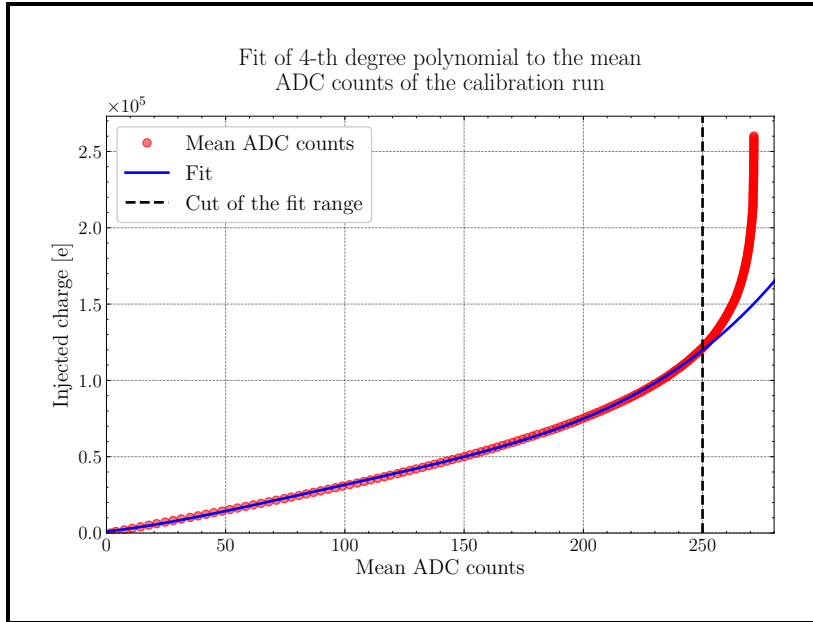


**Figure 3.8:** Injected charge and corresponding ADC counts. A forth degree polynomial function is fitted to the data.

The fit yields the following coefficients:

$$\begin{aligned}
 a &= (5.3 \pm 0.4) \times 10^{-5} e \\
 b &= (-1.91 \pm 0.21) \times 10^{-2} e \\
 c &= (2.7 \pm 0.4) e \\
 d &= (1.75 \pm 24) \times 10^2 e \\
 e &= (9.8 \pm 0.5) \times 10^2 e
 \end{aligned}$$

These coefficients together with [equation \(3.1\)](#) now allow any ADC counts to be converted into an electric charge.

## 3.4 Characteristics of the strip sensor

Geometric parameters of the detector, particularly strip pitch and width, were determined through controlled laser excitation of the sensor. Prior to these measurements, precise temporal synchronization between the laser pulse and readout electronics was established. This synchronization was optimized by systematically varying the trigger delay while monitoring the resulting ADC counts. By definition, the optimal delay time produces the most intense signal, therefore, by looking at [Figure 3.9](#), its value can be set to 110 ns.

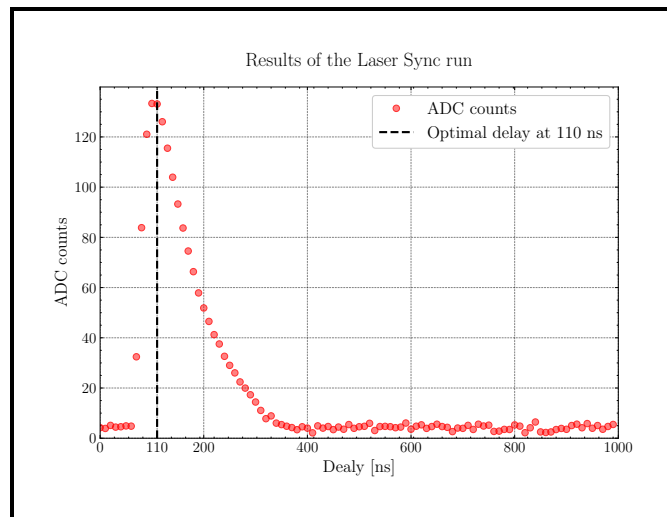


**Figure 3.9:** Results of the *laser sync* run.

After laser-readout synchronization, the laser was translated across the detector surface in 10  $\mu\text{m}$  increments while recording ADC responses at each position. The resulting spatial profile of ADC counts is presented in [Figure 3.10](#) and [Figure 3.11](#), revealing localized signal maxima corresponding to individual sensor strips.

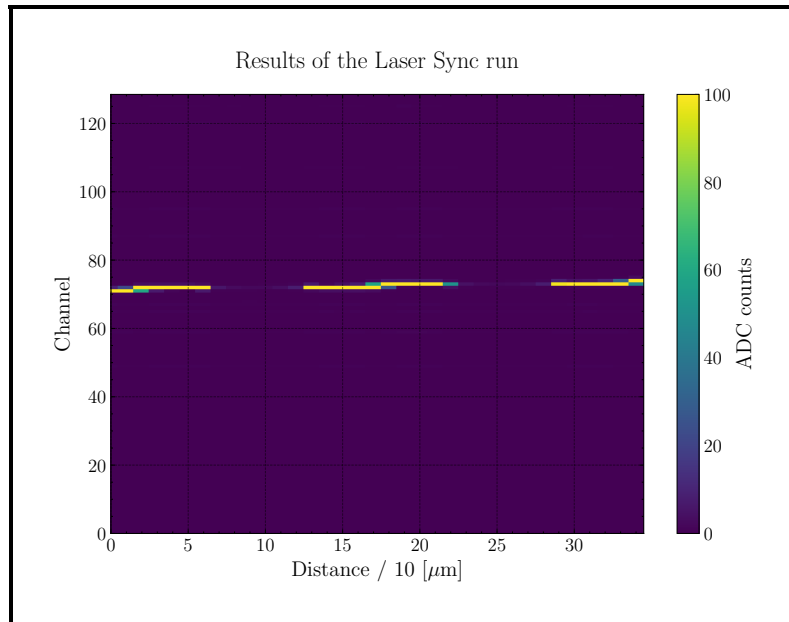


**Figure 3.10:** Heatmap of the signal strength of all the channels depending on the laser position.

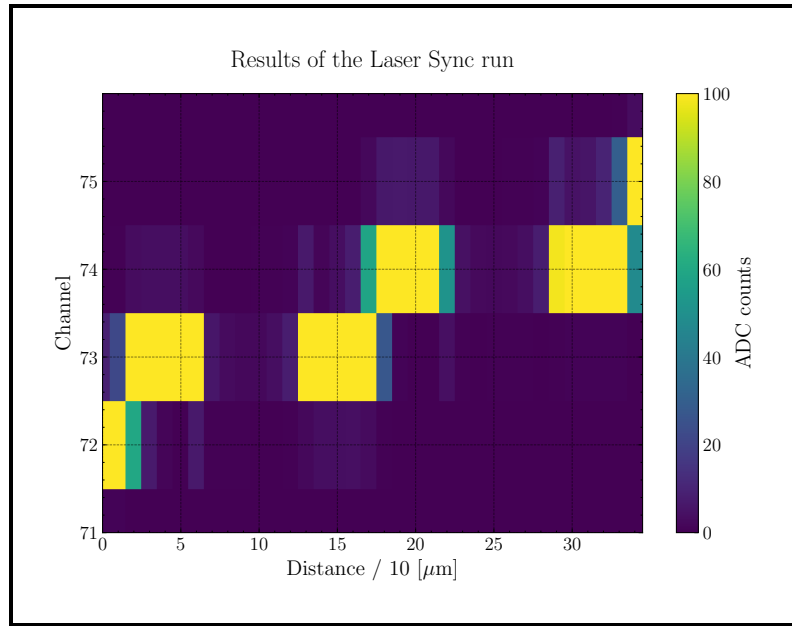


**Figure 3.11:** Heatmap of the signal strength of the affected channels (73, 74) depending on the laser position.

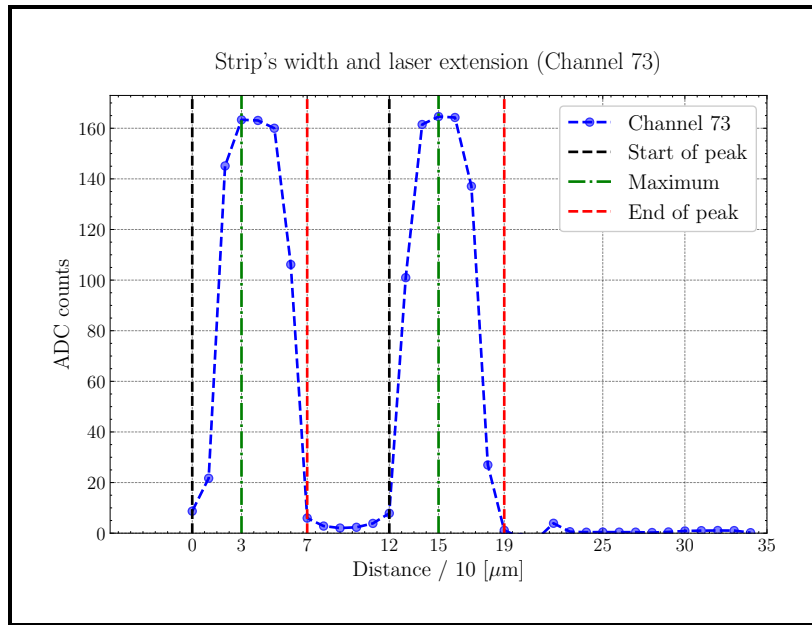


**Figure 3.12:** Signal strength of channel 73 depending on the laser position.

Analysis of the spatial distribution identifies channels 73 and 74 as exhibiting pronounced signal peaks. The ADC responses from these channels (detailed in [Figure 3.12](#)

and [Figure 3.13](#)) provide the strip pitch, by measuring the spatial separation between adjacent response maxima. The width of the laser beam follows from the distance between the minimum and maximum of a peak.

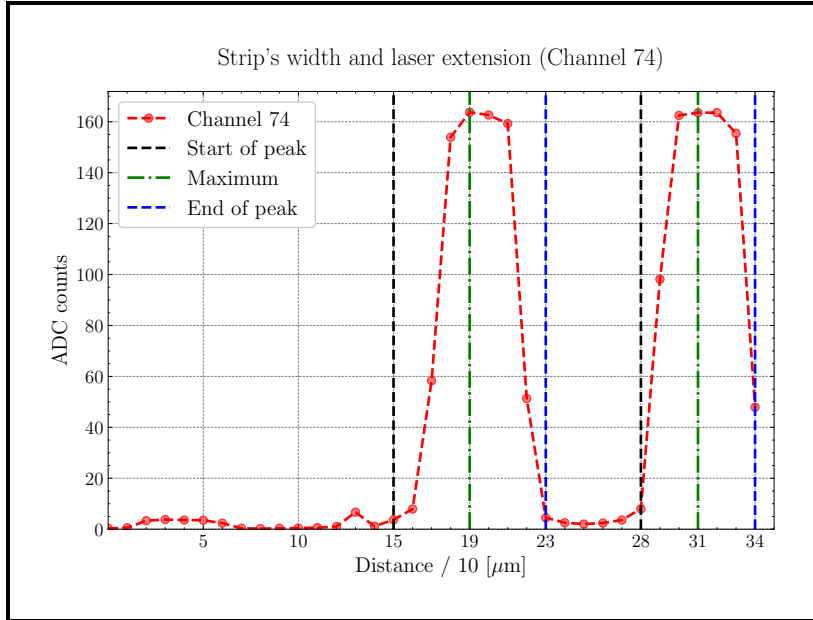


**Figure 3.13:** Signal strength of channel 74 depending on the laser position.

The width of the strip is the distance between the two peaks; the extension of the laser can be estimated by the distance between the start of a peak and its maximum and the distance of two strips can be determined by comparing the position of the maxima of two different channels. The pitch is then calculated as the sum of the distance between the strips and their width:

$$\text{width of strips} = 150 - 30 \text{ (ch73)} = 310 - 190 \text{ (ch74)} = 120 \mu\text{m}$$

$$\text{laser extension} = 150 - 120 \text{ (ch73)} = 310 - 280 \text{ (ch74)} = 30 \mu\text{m}$$

$$\text{distance of strips} = 190 \text{ (ch74)} - 150 \text{ (ch73)} = 40 \mu\text{m}$$

$$\text{pitch} = 120 - 40 = 160 \mu\text{m}$$

### 3.5 Charge Collection Efficiency

In this part of the analysis, the charge collection efficiency (CCE) of the laser is determined in two ways: first, the laser is used to excite the sensor; second, while a  $\beta^-$  source is employed later.

### 3.5.1 CCEL (laser)

When using the laser to excite the sensor, in first place it necessary to determine which channel the laser is focused on. By plotting a heatmap of the ADC counts for each channel, we can see that the laser was focused on channel 72, [Figure 3.14](#) and [Figure 3.15](#).

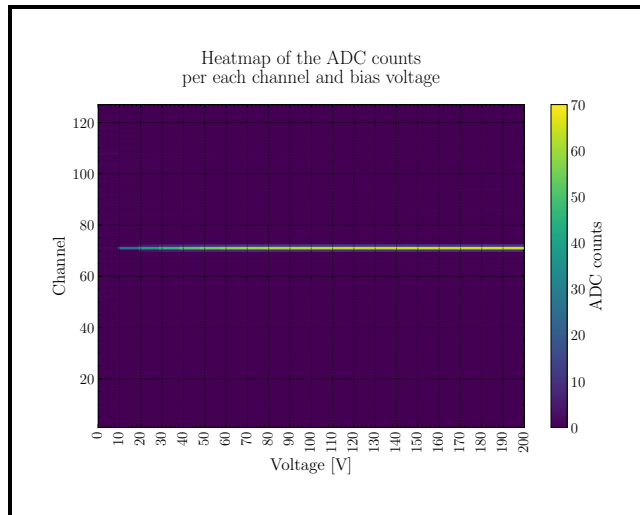


**Figure 3.14:** Heatmap showing the ADC counts of each channel and bias voltage.

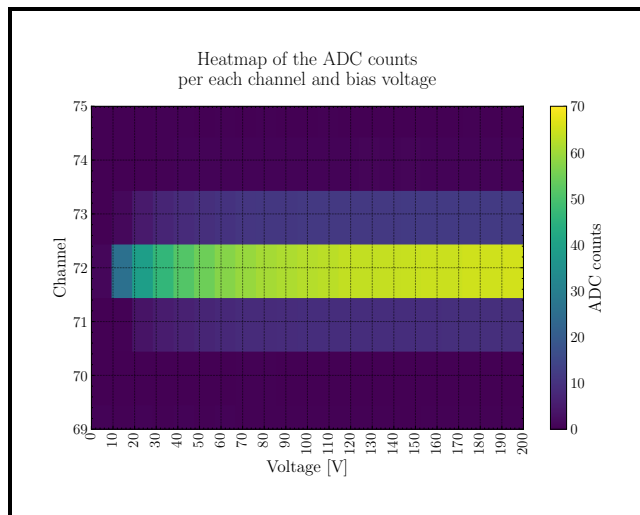


**Figure 3.15:** Zoomed heatmap showing the ADC counts of channel 72 and bias voltage.

To determine the laser penetration depth, [equation \(2.1\)](#) was fitted to the data from channel 72. This required normalization of ADC values relative to their maximum

expected response. Theoretical models predict a constant plateau in ADC counts for bias voltages exceeding the depletion voltage ( $U_{dep}$ ). However, observed plateau regions exhibited minor non-constant behavior due to experimental imperfections. To address this, normalization was performed in regard to the first value of the plateau. The fitting procedure was performed in the range  $0V < U < 80V$ . Within this domain, the depletion voltage  $U_{dep} = 80$  V was maintained as a fixed parameter, so this yielded a penetration depth of:

$$a = (252 \pm 72)\mu\text{m}$$

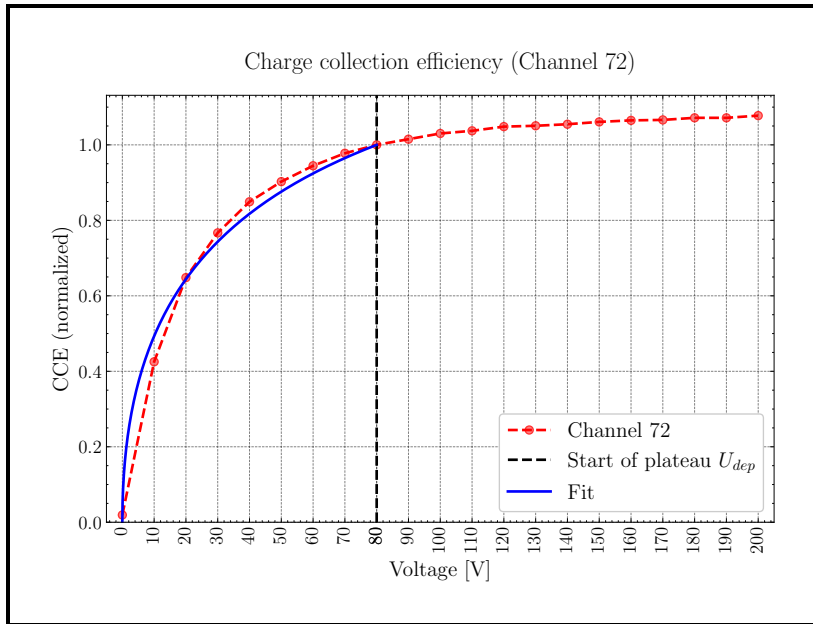


**Figure 3.16:** Charge collection efficiency of channel 72.

### 3.5.2 CCEQ (beta source)

Analogously to the previous analysis step, the measurement of the CCE with a  $\beta^-$  source yields a plot of the ADC counts in dependence of the bias voltage. The mean value across all detected clusters was subsequently calculated to determine charge collection efficiency. This value underwent normalization identical to the laser-based measurement protocol. The resultant characteristic curve depicting system response is presented in Figure 3.17.

In Figure 3.18 we can see that the curve obtained through laser excitation exhibits an earlier response to increasing bias potential compared to the radioactive source method. Both profiles converge completely beyond the depletion voltage threshold. This behavior indicates reduced detection efficiency for charged particles at lower

voltages compared to laser photons. When operating above the critical depletion voltage, this discrepancy becomes negligible as both measurement techniques demonstrate identical charge collection characteristics.

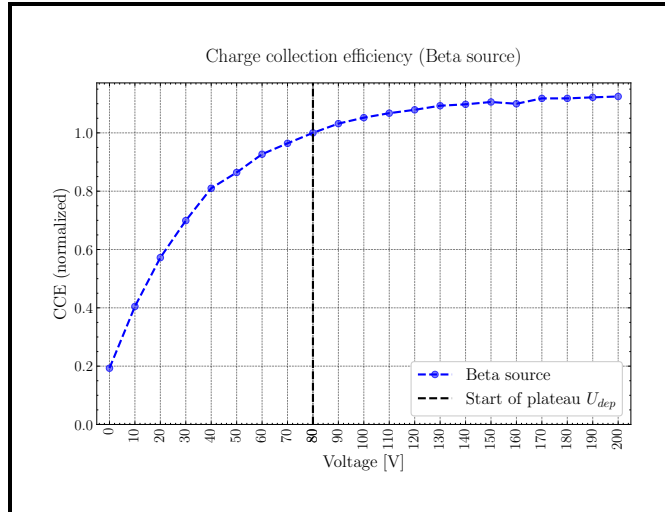


**Figure 3.17:** Charge collection efficiency determined via the  $\beta^-$  source.

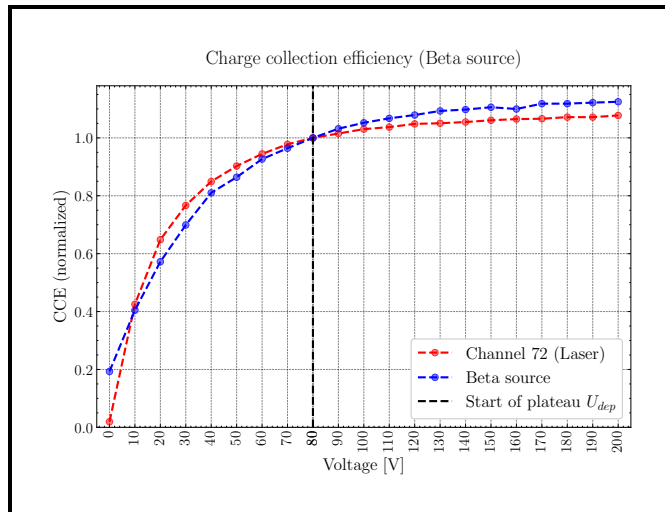


**Figure 3.18:** Comparison of the charge collection efficiency determined via the laser and the  $\beta^-$  source, respectively.

### 3.6 Large source scan

For the last measurement, 1,000,000 events are recorded in the  $\beta^-$  source configuration. Two relevant quantities are recorded and plotted in [Figure 3.19](#) and [Figure 3.20](#): the number of clusters per event and the the number of channels per cluster. Since there is a possibility that more than one channel is fired within the same cluster, one can conclude that the trajectory of electrons is not always perpendicular to the plane of the strips.

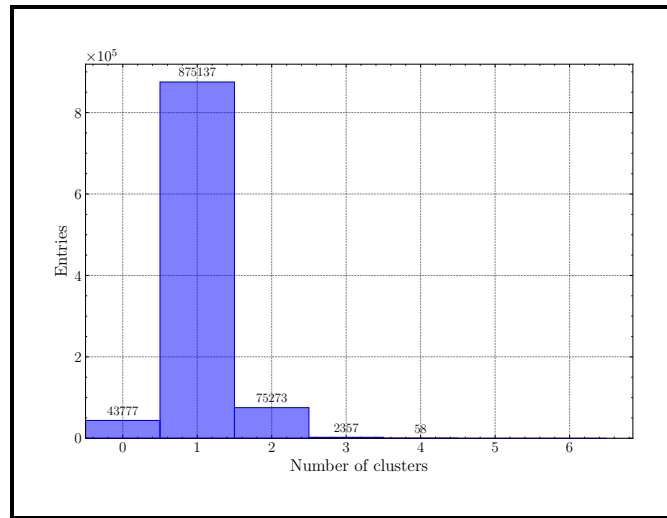


**Figure 3.19:** Number of clusters per event.

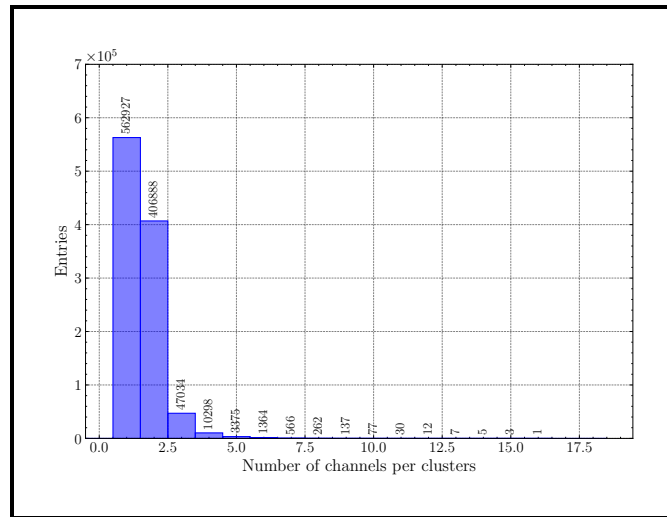


**Figure 3.20:** Number of channels per cluster.

Following, the plot of the distribution of the number hits for each channel during the run, in [Figure 3.21](#). Note: the central channels are the ones being hit most frequently since they are aligned with the radioactive source.

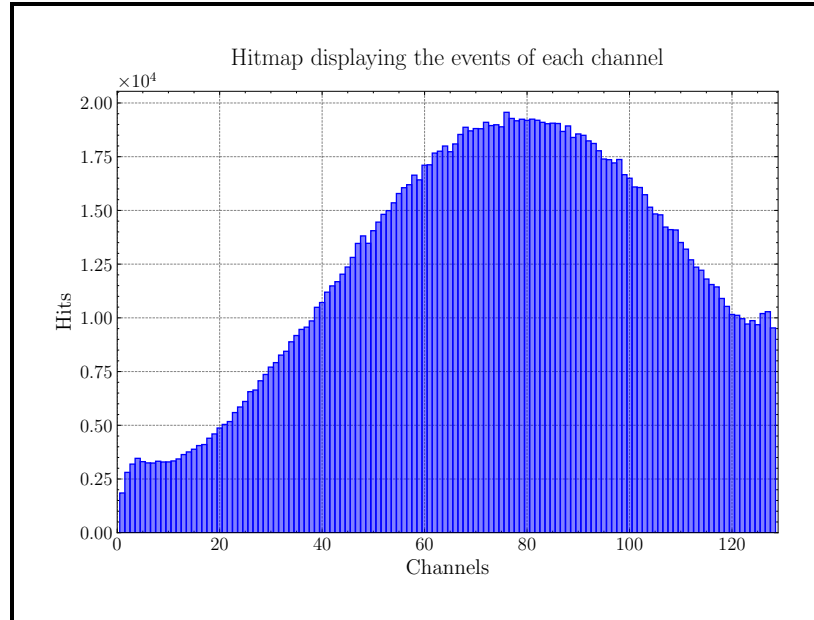


**Figure 3.21:** Hitmap displaying the events of each channel.

The spatial hit distribution exhibits pronounced centrality, with the highest event density occurring near the sensor's geometric center and diminishing toward peripheral regions. Subsequently, statistical distributions of both raw ADC measurements and derived energy values were computed. To transform ADC counts into physical energy values, the conversion relationship established during calibration, [equation \(3.1\)](#), was first applied to obtain equivalent charge pulses. These pulse magnitudes were then converted to energy units using the fundamental silicon ionization energy of 3.6 eV required to create an electron-hole pair. The resulting distributions for both ADC counts and energy spectra are presented collectively in [Figure 3.23](#).

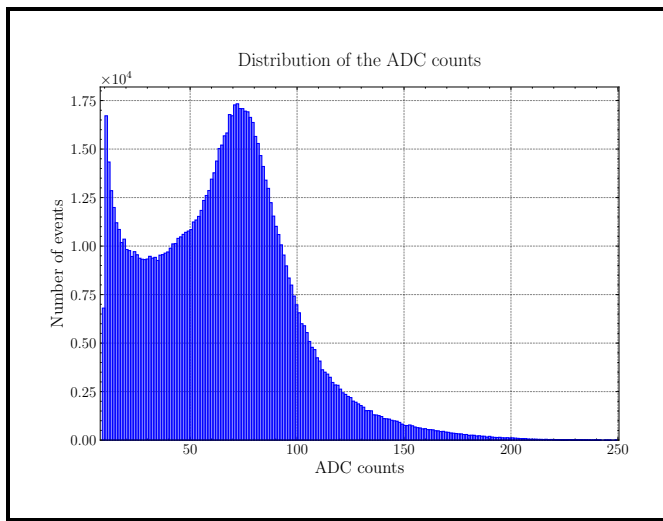


**Figure 3.22:** Distribution of the ADC counts.

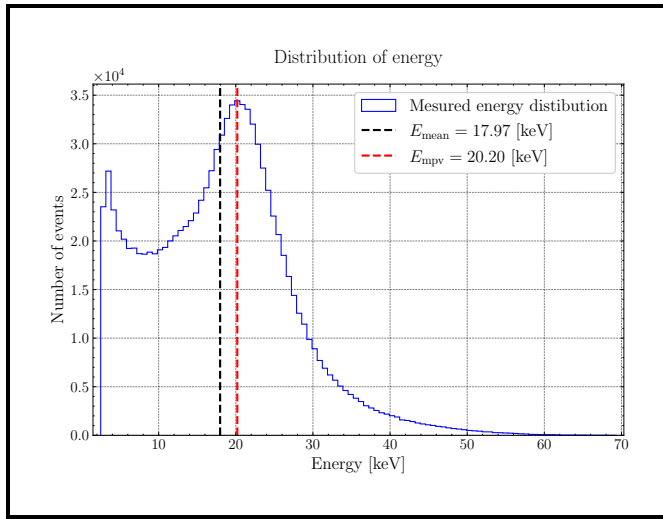


**Figure 3.23:** Energy distribution of the  $\beta^-$  source.

Analysis of the spectral energy distribution enables derivation of characteristic energy parameters for the  $\beta^-$  source:

$$E_{\text{mean}} = 17.97 \text{ keV}$$

$$E_{\text{mpv}} = 20.20 \text{ keV}$$

where  $E_{\text{mpv}}$  denotes the most probable energy (peak value) and  $E_{\text{mean}}$  represents the mean energy.

# Conclusions

This experimental investigation focused on characterizing the operational properties of a silicon radiation detector using both optical excitation (laser) and a radioactive ( $^{90}\text{Sr}$ ) source. Initial calibration procedures preceded the determination of geometric parameters for the detection system. The strip separation was evaluated as  $40\ \mu\text{m}$ , while the laser beam diameter was measured at  $30\ \mu\text{m}$ .

Comparative analysis of detector responses revealed distinct signal characteristics between excitation sources:  $\beta$  decay events from the radioactive source produced lower-amplitude signals compared to laser-induced excitations, attributable to the electron emission in radioactive decay processes. The mean laser penetration depth in silicon was quantified as  $a = (252 \pm 72)\mu\text{m}$ .

Subsequent signal processing involved converting pulse-height distributions from ADC units to energy values in keV. The resulting energy distribution conformed to a Landau profile, with a most probable value of 20.20 keV and a mean energy of 17.97 keV.